Submitted to the colloquium:

Spray, Droplet and Supercritical Combustion

Length of the paper determined using method 2

Total length of the paper: **7.5 pages**

Total length of the abstract: **213 words**

Numerical study of multicomponent spray flame propagation

Varun Shastry*, Quentin Cazeres, Bastien Rochette, Eleonore Riber,
Bénédicte Cuenot

42 Avenue Gaspard Coriolis, Toulouse Cedex 1, 31057, France

Abstract

A computational study of one dimensional multicomponent laminar Jet-A/air spray flames is presented. The objective is to understand the effect of various spray parameters (diameter, droplet velocity, liquid loading) on the spray flame structure and propagation. Simulation of the Eulerian gas phase is coupled with a Lagrangian tracking of the dispersed liquid phase. Jet-A surrogate of n-dodecane, methyl-cyclohexane and xylene is considered. A discrete multicomponent model for spray vapourisation is used along with an analytically reduced chemistry for computing the gas phase reactions. Both overall lean and rich cases are examined and compared with existing literature for single component spray flames. The preferential evaporation effect, unique to multicomponent fuels cause a variation of fuel vapour composition on both sides of the flamefront and this has a direct impact on the spray flame structure and propagation speed. In rich cases, multiple flame structures exist due to the staged release of vapours across the reactive zone. Spray flame speed correlations proposed for single component fuels are ex-

---

*Corresponding author
  Email address: `varun.shastry@cerfacs.fr` (Varun Shastry)

tended to the multicomponent case, for both zero and high relative velocity between the liquid and gas. The correlations are able to accurately predict the effective equivalence ratio at which the flame burns and hence the laminar spray flame speeds of multicomponent fuels for all cases studied in this work.

1. Introduction

Spray formation and combustion have been extensively studied due to the wide ranging application in propulsion and power generation[1]. The various mechanisms involved, occurring at different length and time scales lead to a very complex combustion process with multiple flame structures and combustion regimes [2]. Large Eddy Simulations coupled with detailed chemistry descriptions have been recently performed to get an insight into these highly coupled systems. However a single component representation of the liquid fuel has been mostly utilised [3–5].

Real fuels used in these combustion systems contain a large number of components belonging to a range of hydrocarbon families. Differences in their volatilities cause a spatio-temporal variation of the reactive gas phase mixture as the spray evolves. Additionally, preferential evaporation significantly affects the mixture reactivity specially when vaporisation and autoignition time-scales are comparable and in the presence of turbulent structures [6, 7]. To address these, a detailed study of multicomponent spray flame structure and propagation is thus necessary in understanding turbulent combustion of

3

fuel blends and developing corresponding models in addition to the existing LES studies [8].

To the authors knowledge, little literature exists on multicomponent laminar spray flames and the parameters influencing it. The one dimensional laminar premixed spray flame configuration using a single component fuel has been studied to understand the main propagation mechanisms. For lean and stoichiometric mixtures, Ballal and Lefebvre [9] experimentally showed that compared to a gaseous premixed laminar flame at the same overall equivalence ratio, increasing droplet diameter reduces the laminar spray flame speed. This is due to the vapourisation of smaller droplets before reaching the flamefront, which increases the equivalence ratio seen by the flame. For rich mixtures, Hayashi et al. [10] observed an enhanced flame speed over a specific range of droplet diameters in rich mixtures. Here the partial evaporation causes the mixture to burn at stoichiometric conditions enhancing the flame speed. Based on detailed chemistry simulations, Neophytou and Mastorakos [11] marginally correlated the laminar spray flame speed trends with an effective equivalence ratio ϕ_{eff} seen by the flame. All of these studies were performed for zero relative velocity between the liquid and the gas phases. However recently, Rochette et al. [12] performed one dimensional n-heptane laminar spray flame simulations using a two-step chemistry and showed that the relative velocity between the liquid phase and the carrier gas phase also has significant impact on ϕ_{eff} and hence the propagation speed. They also derived correlations for the estimation of ϕ_{eff} and the laminar spray flame speed as a function of the spray parameters.

This work aims to analyse the effect of a multicomponent fuel on spray

flames, including evaporation and chemistry effects. It is the first attempt to include both Analytically Reduced Chemistry (ARC) and multicomponent evaporation in one dimensional numerical simulations to understand the effect of various spray parameters (diameter, liquid loading, relative velocity and equivalence ratio) on the structure and propagation of a multicomponent spray flame.

2. Numerical setup

Computations are performed using the CFD code AVBP with a Lagrangian point particle formulation to represent the spray. Source terms for transfer of mass, momentum and energy from the liquid to gaseous phase are distributed to the closest nodes in the Eulerian gas phase in a two-way coupling approach (http://cerfacs.fr/avbp7x/).

Chemical Mechanism

In this work, the surrogate for Jet-A proposed by Narayanaswamy et al. [13] is reduced. The three components of the surrogate are n-dodecane (NDC), methyl-cyclohexane (MCH) and a xylene (XYL) species that represents the three possible isomers (ortho-, para- and meta-xylene). The mole fractions of each component in the fuel are $X_{NDC} = 0.451$, $X_{MCH} = 0.268$ and $X_{XYL} = 0.281$. The detailed mechanism with 230 species and 4868 reversible reactions of [14] has been reduced with reduction code ARCANE (https://chemistry.cerfacs.fr/en/arcane/) based on YARC [15]. The resulting mechanism, **JetA_3Comp_45_686_16_QC**, comprising of 45 transported species, 16 Quasi-Steady State species and 686 irreversible reactions is provided in the supplementary material. The **JetA_3Comp_45_686_16_QC**

5

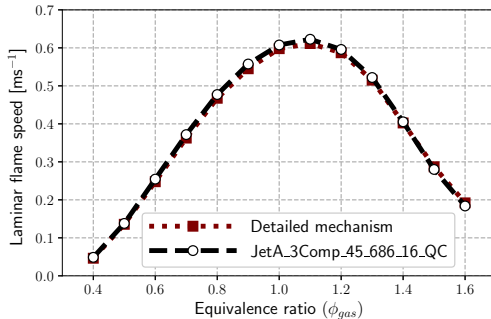scheme for the surrogate is in very good agreement with the detailed mechanism for premixed flames on the whole equivalence ratio range at $400\,\mathrm{K}$ and $1\,\mathrm{bar}$ as shown in Fig. 1.

Fig. 1: Laminar flame speed for gaseous mixture of Jet-A surrogate/Air at $400\,\mathrm{K}$ and $1\,\mathrm{bar}$

Droplet Evaporation Model

The droplet evaporation is modelled using a quasi steady state assumption. Detailed description of the evaporation model can be found in earlier studies [3, 12]. The multicomponent extension is discussed here. The Spalding mass transfer number B_M and the fraction of vapour ϵ^i for an individual component i are calculated as [1]:

$$B_M = \frac{\sum_{i=1}^{k} Y_{surf}^i - \sum_{i=1}^{k} Y_{\infty}^i}{1 - \sum_{i=1}^{k} Y_{surf}^i} = \frac{Y_{surf}^i - Y_{\infty}^i}{\epsilon^i - Y_{surf}^i} \tag{1}$$

where Y^i is the mass fraction of the individual component i and the subscripts $surf$ and ∞ denote the droplet surface and far-field locations respectively. Only the components present in the liquid phase are considered in Eq. 1.

Vapour liquid equilibrium Eq. 2 is used to obtain the mole fractions of the fuel components at the droplet surface $(X_{i,surf})$ using the liquid mole

6

fractions ($X_{i,liq}$) and the vapour pressure ($P_{sat,i}(T)$) of the different components. Calculating the surface mass fractions Y^i_{surf} to be used in Eq. 1 is then straightforward.

$$X_{i,surf}P_{gas} = X_{i,liq}P_{sat,i} \tag{2}$$

Using the above equations, the evaporation rate m^i_p of an individual component can be calculated using the total evaporation rate of the droplet $\dot{m}_p$ and the fraction of vapour ϵ_i as:

$$\dot{m}^i_p = \epsilon^i \dot{m}_p \quad \text{with} \quad \sum_{i=1}^{k} \epsilon^i = 1 \tag{3}$$

The unsteady effects encountered in the multicomponent evaporation include the heat diffusion and mass diffusion in the liquid phase. Time scales for droplet heating(τ_H) and droplet evaporation (τ_{ev}) can be compared using the specific heat capacities (c) and thermal conductivity (λ) of the liquid(liq) and gaseous(gas) phases as

$$\frac{\tau_H}{\tau_{ev}} = \mathrm{O}\left(\frac{\lambda_{gas}c_{liq}}{\lambda_{liq}c_{gas}}\right) \tag{4}$$

For droplets exposed to high temperature, $\tau_H < \tau_{ev}$, causing the droplet to reach the steady wet bulb temperature. A similar analysis comparing the mass diffusion inside the liquid (τ_{diff}) with the droplet evaporation (τ_{ev}) in terms of the diffusion coefficient (D) and density(ρ) yields

$$\frac{\tau_{diff}}{\tau_{ev}} = \mathrm{O}\left(\frac{D_{gas}\rho_{gas}}{D_{liq}\rho_{liq}}\right) \tag{5}$$

Since $D_{liq} \ll D_F$ the time scales in this case be comparable. The more volatile components on the droplet surface quickly evaporate in the high

temperatures. This sets up a very strong gradient especially for the small droplets and a flux from the centre to surface. For droplet diameters of $100\mu m$ (greater than range used in this work) little differences in the evaporation trends was observed for multicomponent droplets modelled with these unsteady effects [16] and an infinite liquid diffusivity(used here).

The implemented is able to capture the major trends of multicomponent droplet evaporation (evaporation timescales, preferential evaporation), shown in Fig. 2 by the evolution of Normalised diameter(ND) and temperature for single evaporating droplet. After an initial heating phase, the droplet surface area reduces linearly following the D^2, agreeing well with the experimental data of [17]. The varying composition of the vapour flux is shown in Fig. 2, it can be observed the highly volatile MCH dominates the composition initially. As the relatively volatile MCH and XYL completely evaporate, the liquid and vapour composition in the latter part is solely composed of NDC.

Under saturated conditions and in flame regions it is possible to encounter isolated single droplet combustion. The diameter of flame(d_f) around a droplet of size(d_p) in this regime can be calculated using the mass fraction of oxidiser in the far field conditions(Y_{Ox}^∞) [1]
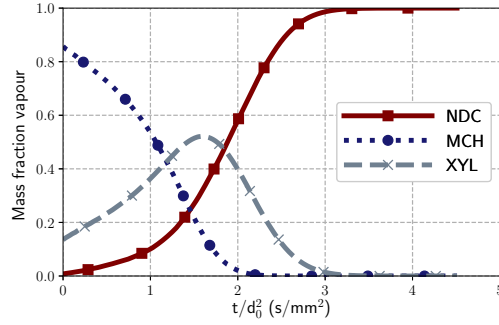
$$d_f = d_p \frac{\ln\left(1 + B_M^{comb}\right)}{\ln\left(1 + Y_{Ox}^\infty\right)} \tag{6}$$

In the flame zone with B_M^{comb} of 3.3 we obtain $d_f \approx 12d_p$. When the interdroplet distance $S < d_f$, the isolated droplet burning regime is not reached.

8
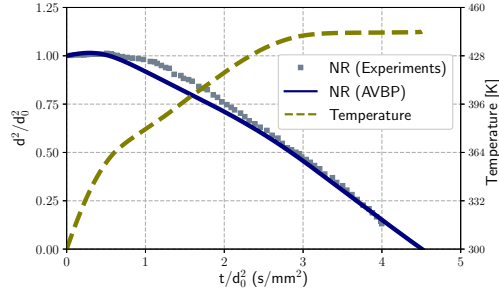
(a) Evolution of Normalised Diameter and temperature

(b) Varying composition of the evaporating flux

Fig. 2: Temporal evolution of the vapour flux composition for single Jet-A droplet of initial diameter and temperature $1000\,\mu$m and $300\,$K evaporating in a quiescent air at $773\,$K
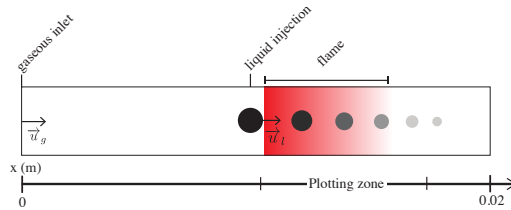
Configuration

Fig. 3: Computational configuration [12]

The one-dimensional domain shown in Fig. 3 is $0.02m$ long and is discretised using 500 equally spaced elements. To avoid the influence of droplet

residence time and for better control of the liquid and gaseous fluxes into the reaction zone, fuel droplets are injected just in front of the flame. Interaction of the fuel droplets and the premixed flame causes a change in flame speed and position. The inlet velocity (u_g) must be adjusted to a new value of the two-phase laminar flame speed $S_{L_{TP}}$ stabilize the flame.

The simulated cases are summarised in Tab. 1 . Cases A and B represent overall lean and rich cases. Case C is overall lean and only liquid fuel is provided to the flame. All three cases are representative of the combustion regimes that may occur in three dimensional turbulent spray flames. The total equivalence ratio describes the overall fuel-to-oxidizer ratio, the ratio of the total fuel (gaseous and liquid) to the total oxidizer injected in the domain, $((m_{fuel}^{liq} + m_{fuel}^{gas})/m_{ox})$. The total equivalence ratio hence is represented as the sum of gaseous and liquid equivalence ratios ($\phi_{\text{tot}} = \phi_{\text{gas}} + \phi_{\text{liq}}$).

Cases A to C have been set-up to cover a wide range of typical burning regimes observed in real combustors where preferential concentration may lead to a variety of both local liquid loadings and gaseous equivalence ratios. Moreover, the effect of relative velocity has been investigated to get even closer to real operating conditions where the relative velocity between the gas and droplets can be high as the air and liquid fuel injections are separate.

Inlet gas temperature is 400K and droplets are injected at 300K. The flame speeds and structures are computed over a range of droplet diameters ranging from $d_p = 5\mu m$ to $80\mu m$. For a given droplet diameter, the number of injected droplets is adjusted to fulfil the targeted equivalence ratio. The isolated burning droplet regime is unreachable in this set-up as the inter-droplet distance is less than d_f introduced previously. The relative velocity

10

between the phases is taken into account by introducing a velocity ratio
$u^* = u_{liq}/u_{gas}$ [12].

Case name	ϕ_{tot}	$\phi_{gas,liq}$	u^*	d_p (μm)
A	0.9	$\phi_{gas} = 0.8$ $\phi_{liq} = 0.1$	1, 30	5-80
B	1.3	$\phi_{gas} = 0.8$ $\phi_{liq} = 0.5$	1, 30	5-80
C	0.9	$\phi_{gas} = 0.0$ $\phi_{liq} = 0.9$	1, 30	5-80

Table 1: Conditions of simulated cases

Results

Multicomponent spray flame structure

Flame structures for the cases in Tab. 1 are compared for $d_p = 20\mu m$, $u^* = 1$ and 30. The heat release (HR) profiles are plotted with the evaporation source terms (Γ_F) and the volumetric consumption ($-\dot{\omega}_F$) speed of the components. Droplets injected just before the flamefront begin to release vapour in the reacting zone and the evaporation zone extends beyond the main flame region.

In Fig. 4 for Case A and $u^* = 1$ MCH is shown to evaporate completely in the main flame region followed by XYL and finally NDC. The preferential evaporation of MCH and its complete consumption within the main premixed flame zone shown in Fig. 4b causes a slight increase in ϕ_{eff} compared to ϕ_{gas}. As the droplets move through the main flamefront gradually they contain only XYL and NDC, and finally only NDC, whose evaporation rate reaches a maximum in the post-flame high temperature region. Due to the lower

11

volatility and longer evaporation distance of NDC, a secondary consumption zone with very low but non-zero reaction rates exist as seen in Fig. 4c.

Increasing the droplet velocity so that $u^* = 30$ shifts the evaporation zone behind the main flamefront as shown in Fig. 5. The dominant flame structure

140 is that of the premixed gaseous flame at $\phi_{gas} = 0.8$ and the contribution of the liquid phase towards ϕ_{eff} is negligible. An extended secondary combustion zone behind the main reaction zone exists where the evaporating droplets react with the excess oxygen. This zone for NDC is shown in Fig. 5b, and similar ones for MCH and XYL are observed (not shown).

145 In Case A two limiting regimes may be encountered. The first corresponds to droplets small or slow enough to evaporate completely in the main reaction zone leading to $\phi_{eff} = \phi_{tot}$ while in the second limit large or fast droplets contribute very little to the flame propagation and $\phi_{eff} = \phi_{gas}$. As the flame is overall lean, this leads to the spray flame speed limits for Case A to lie

150 between $S_{L_{\phi gas}} \leq S_{L_{TP}} \leq S_{L_{\phi tot}}$.
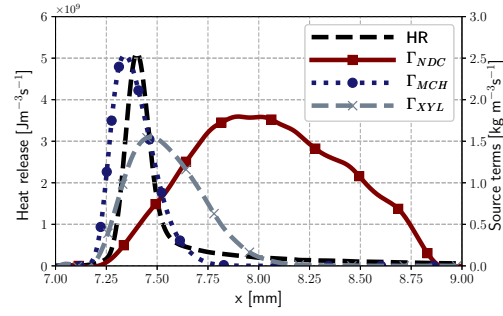
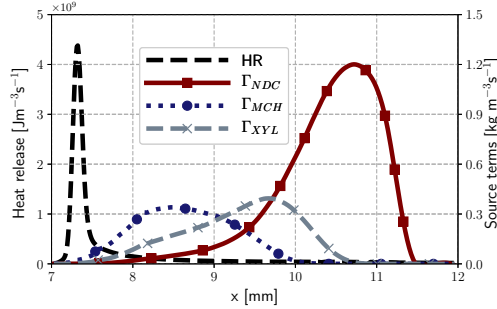(a) Heat release and evaporation source terms
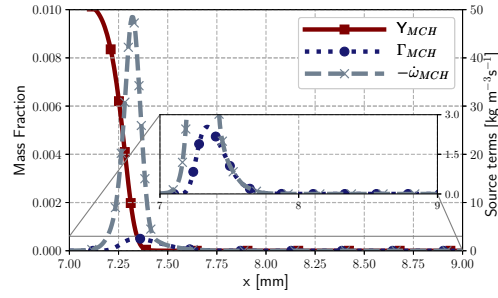
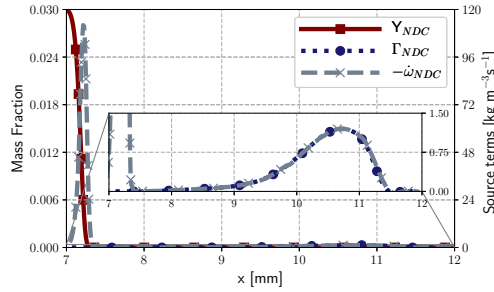(b) Mass fractions and consumption rates of MCH
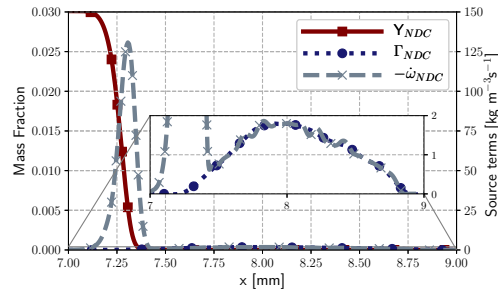
(c) Mass fractions and consumption rates of NDC

Fig. 4: Profiles of heat release, mass fractions, evaporation and consumption rates for Case A, $d_p = 20\mu m$ and $u^* = 1$

13

(a) Heat release and evaporation source terms
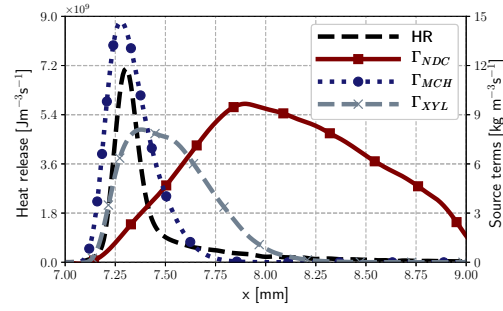

(b) Mass fractions and consumption rates of NDC

Fig. 5: Profiles of heat release, mass fractions, evaporation and consumption rates for Case A, $d_p = 20\mu m$ and $u^* = 30$

The spatial profiles of HR, Γ_F and $-\dot{\omega}_F$ for Case B are shown in Fig. 6 and Fig. 7. The evaporation trends are very similar to Case A, however due to the high liquid loading the amount of vapour released is significantly higher. For the condition $u^* = 1$ the evaporation and consumption profiles of MCH (not shown) are similar to that observed in Fig. 4b. NDC shows a strong and prominent secondary reaction zone behind the main premixed flamefront where the remaining oxidiser is consumed in long droplet burning regime highlighted in Fig. 6b. As in Case A, this secondary reaction zone does not affect the propagation speed but contributes towards the overall

14

heat release.

For $u^* = 30$, a distinct secondary reaction zone away from the premixed flamefront is observed for NDC. Since the main premixed flame is lean with $\phi_{\text{gas}} = 0.8$, the remaining oxidiser is consumed as the evaporation progresses. Multiple reaction pathways are possible for the consumption of fuel components due to the ARC mechanism used. Some vapour released in this region also undergo pyrolysis producing new smaller fuel species which diffuse back to burn with oxygen. This complex diffusion flame structure is illustrated with two components formed by NDC pyrolysis (H_2, C_2H_2) having a slope of opposite sign compared to the oxygen (O_2) profile, in Fig. 7b and the accompanying heat release in shown in Fig. 7c. Burnt gas composition contains the standard combustion products CO_2, H_2O, CO together with smaller components.

As in Case A, the upper and lower limits of ϕ_{eff} for Case B are ϕ_{tot} (fast evaporation) and ϕ_{gas} (slow evaporation). However, with $\phi_{tot} = 1.3$ it is possible to find conditions for which $\phi_{eff} \approx 1.0$ leading to $S_{L_{TP}} > S_{L_{\phi_{tot}}}$.
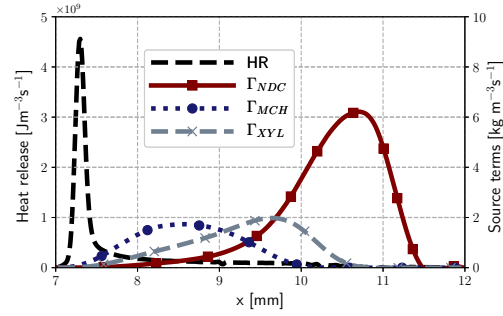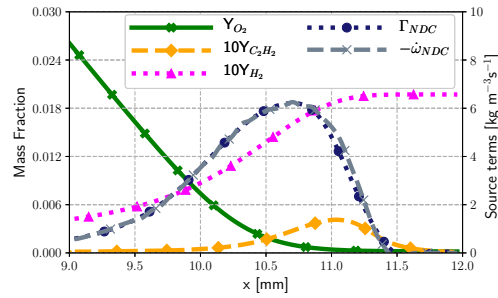
15

(a) Heat release and evaporation source terms
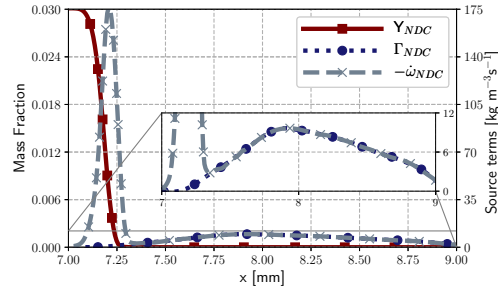
(b) Mass fractions and consumption rates of NDC

Fig. 6: Profiles of heat release, mass fractions, evaporation and consumption rates for Case B, $d_p = 20\mu m$ and $u^* = 1$
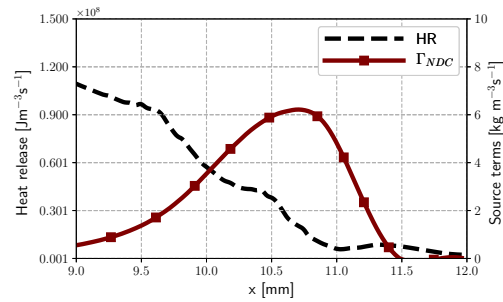
(a) Heat release and evaporation source terms

(b) Diffusion flame structure for NDC

(c) Zoom on heat release and evaporation in the post flame region

Fig. 7: Profiles of heat release, mass fractions, evaporation and consumption rates for Case B, $d_p = 20\mu m$ and $u^* = 30$

Results for Case C where all the fuel is in the liquid phase are shown in Fig. 8 and Fig. 9. For $u^* = 1$, the faster evaporation of MCH initiates the

17

flame. Significant amounts of XYL and NDC also vaporise before the location of peak heat release. Energy from the reactions provides the latent heat of
¹⁸⁰ evaporation needed to sustain the flame. This causes significantly lower heat release rates and flame speeds compared to a purely gaseous flame or spray flame with lower liquid loading as Case A. For higher droplet velocities $u^* = 30$, the reaction zone develops later after significant amount of liquid fuel has vaporised. For the purely liquid controlled Case C, the HR zone
¹⁸⁵ extends across the entire evaporation zone of the droplets with $-\dot{\omega}_F$ and Γ_F superimposed in this region.
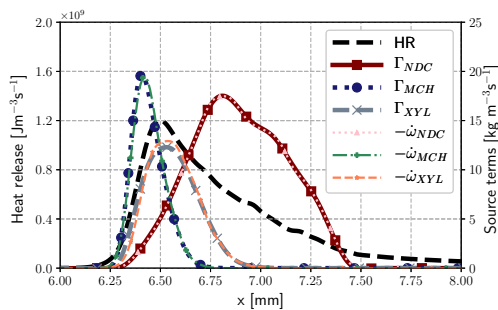

Fig. 8: Profiles of heat release, evaporation and consumption rates for Case C, $d_p = 20\mu m$ and $u^* = 1$

Laminar two-phase flame speeds for multicomponent droplets

Similar to the single component fuel [12], the laminar two-phase flame speed is controlled by ϕ_{eff} which is a function of the gaseous equivalence
¹⁹⁰ ratio and the evaporation of liquid inside the flamefront of thickness δ_L^0. The distance over which the droplets evaporate, compared against δ_L^0 can be used to estimate the contribution of evaporation to ϕ_{eff}. Previously laminar flame speed correlations have been developed and validated for a single component
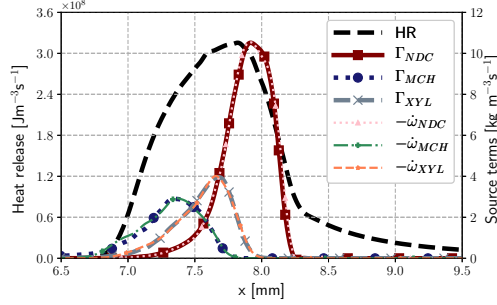
18

Fig. 9: Profiles of heat release, evaporation and consumption rates for Case C, $d_p = 20\mu m$ and $u^* = 30$

n-heptane case [12]. To extend these correlations to the present case, it is necessary to consider the varying evaporation rates and contributions of the liquid fuel components. Such a varying vapour flux for an evaporating Jet-A droplet of $100\,\mu$m at $313\,$K in quiescent air at $500\,$K is shown in Fig. 2.

The different evaporation time scales (τ_{ev}^i), of the liquid components are calculated using the fraction of each component ϵ_i averaged over the lifetime of i in the liquid state. In Eq. 7 the Spalding mass transfer number B_M is calculated at the mean of liquid injection and wet bulb temperatures, $(T_{inj} + T_{wb})/2$ (using the T_{wb} of NDC in this case because it is the last remaining component) for a droplet evaporating in flame conditions.

$$\tau_{ev}^i = \frac{\rho_{liq}d_{p0}^2}{12\rho_{gas}D_F\epsilon_i \ln\left(1 + B_M\right)} \underbrace{\left[1 + \frac{kSc^{1/3}Re_p^{1/2}}{2\dfrac{(1 + B_M)^{0.7}\ln\left(1 + B_M\right)}{B_M}}\right]^{-1}}_{\text{accounts for droplet velocity}} \tag{7}$$

where d_{p0}, ρ_{liq} and ρ_{gas} are the initial droplet diameter, liquid and gas density respectively. D_F is the diffusion coefficient of the fuel vapour, Sc is the

Schmidt number of the surrounding gas and Re_p is the Reynolds number of the droplet. k is a factor whose value is taken as 0.6. [1].

For droplets with high relative velocity, it is important to take into account drag force acting on them. Using the droplet relaxation time $\tau_p = \rho_{liq} d_{p0}^2 / 18 \mu_{gas}$ (μ_{gas} is the dynamic viscosity of the surrounding gas) and the flame time $\tau_f = \delta_{S_L}^0 / S_L^0$, a flame Stokes number is identified as $St_f = \tau_p / \tau_f$. A droplet injected with a velocity u_{p0} reaches after crossing the flame thickness the velocity u_p:

$$u_p = u_{gas} \left(1 - e^{-1/St_f}\right) + u_{p0} e^{-1/St_f} \tag{8}$$

The evaporation length for each component i is then given by $\delta_{ev}^i = u_p \tau_{ev}^i$. Following Rochette et al. [12] and using the above expressions, ϕ_{eff} is

$$\phi_{eff} = \sum_i \left(\frac{\delta_L^0}{max\left(\delta_L^0, \delta_{ev}^i\right)}\right)^{\frac{2}{3}} \left(\frac{s_i}{s_{Jet\text{-}A}}\right) \phi_{liq} + \phi_{gas} \tag{9}$$

In Eq. 9, s is the stoichiometric ratio. For a hydrocarbon fuel $C_x H_y$, $s = x + y/4$. The term $s_i / s_{Jet\text{-}A}$ accounts for the varying contribution of each component present in the liquid fuel to ϕ_{eff}. For small droplets which evaporate fast, Eq. 9 yields $\phi_{eff} = \phi_{tot}$. For larger droplets having non-negligible evaporation times, Eq. 9 gives $\phi_{gas} < \phi_{eff} < \phi_{tot}$. Similarly, volatile components with $\delta_{ev}^i \leq \delta_L^0$ contribute completely to ϕ_{eff} whereas less volatile components with large evaporation thickness only partially contribute to the flame.

For flames controlled by evaporation (Case C), the flame speed correlations from Rochette et al. [12] considering the smallest evaporation timescale of MCH (τ_{ev}^{MCH}) is used.

$$S_L^{TP} = \frac{\delta_{S_{L_{\phi gas}}}}{\tau_{ev}^{MCH}} \tag{10}$$

The correlations are compared with the simulation results for all cases in Tab. 1 and overall a good agreement with the trends are observed. Comparison for Case A is shown in Fig. 10 . The laminar flame speed is less than $S_{L_{\phi_{tot}}} = 0.56\,\mathrm{m}s^{-1}$ for all droplet sizes. For large droplets the contribution of evaporation to ϕ_{eff} is negligible. Increasing the droplet velocity reduces

the residence time in the reactive zone, reducing further the liquid phase contribution leading to $\phi_{eff} = \phi_{gas}$ and $S_{L_{TP}} = S_{L_{\phi_{gas}}} = 0.48\,\mathrm{m}s^{-1}$.
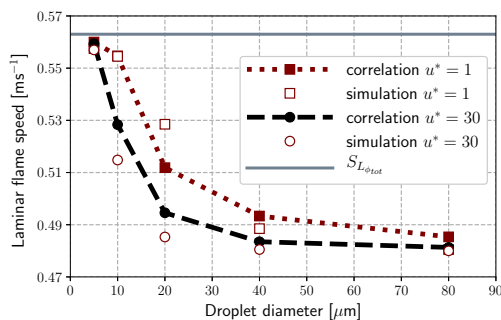

Fig. 10: Two-phase flame speed of Jet-A vs initial droplet diameter. Comparison between simulations and correlations (Eq. 9) for Case A

For Case B (Fig. 11), an optimum diameter exists at which the two phase flame burns close to stoichiometry. For $u^* = 1$ it is found at $20\,\mu$m and for $u^* = 30$ at $10\,\mu$m. Due to the varying volatilities of the multicomponent fuel,

such an optimum diameter exists even when the droplets move very quickly across the flame.
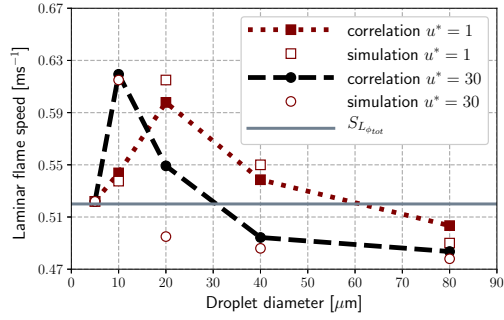
21

Fig. 11: Two-phase flame speed of Jet-A vs initial droplet diameter. Comparison between simulations and correlations (Eq. 9) for Case B
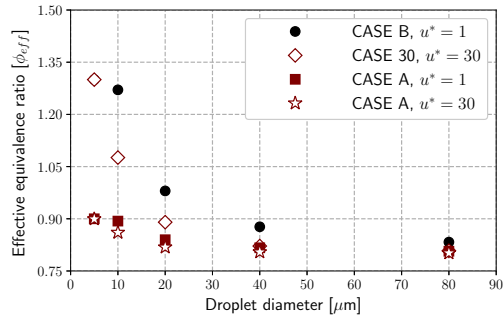

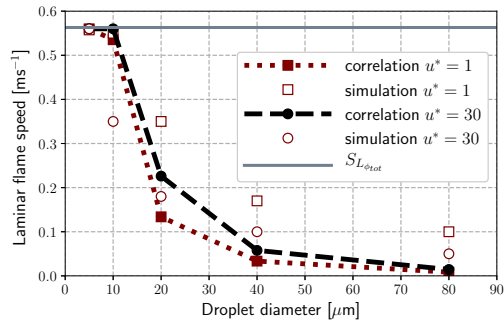Fig. 12: Effective equivalence ration calculated by Eq. 9

Fig. 13: Two-phase flame speed of Jet-A vs initial droplet diameter. Comparison between simulations and correlations (Eq. 10) for Case C

For the evaporation controlled flames of Case C (Fig. 13), correlation follows the trend but with some deviation from the simulation results. It is observed in Fig. 13 that a flame can be sustained for gaseous equivalence ratios lower than the flammability limit if droplets have low or zero relative velocities. As was observed in Fig. 8 and Fig. 9, significant amounts of liquid components evaporate before a stable flame can be sustained. This leads to multiple reaction pathways involving all components, hence τ_{ev}^{MCH} cannot be used alone for the estimation of the flame speed. A detailed comparison between the evaporation and chemical timescales is needed to obtain a better agreement with the simulated data for Case C.

Conclusions

Multicomponent one-dimensional spray flame simulations were performed for a Jet-A surrogate composed of n-dodecane (NDC), methyl-cyclohexane (MCH) and xylene (XYL). Flame structure and spray flame speed have been examined for a wide range of equivalence ratios, droplet diameters and droplet velocities. Due to the varying volatilities of these components, a staged evaporation behaviour was observed as the droplets move through the reactive flamefront. MCH being the most volatile component enhances the effective equivalence ratio and this effect is more pronounced for low relative velocities. NDC being the least volatile component leads to an extended secondary reaction zone following the primary flame zone. For rich cases with high relative velocity, a separated secondary diffusion flame of NDC can even be observed. For purely liquid fuels the heat release zone extends over the entire evaporation zone. Correlations were proposed to es-

23

timate laminar spray flame speeds considering the varying vapour fluxes and contributions of the different liquid components as well as the drag effect. These correlations are in very good agreement with numerical results, except for purely liquid flames which demand an accurate comparison of the various evaporation and chemical timescales and will be the focus of future work. Overall the various mechanisms controlling the laminar spray flame speed for multicomponent droplets have been identified and may be used in turbulent combustion modelling of multicomponent sprays.

Acknowledgments

References

[1] W. A. Sirignano, Fluid dynamics and transport of droplets and sprays, Cambridge University press, 2010.

[2] A. L. Sánchez, J. Urzay, A. Liñán, The role of separation of scales in the description of spray combustion, Proceedings of the Combustion Institute 35 (2015) 1549–1577.

[3] A. Felden, L. Esclapez, E. Riber, B. Cuenot, H. Wang, Including real fuel chemistry in LES of turbulent spray combustion, Combustion and Flame 193 (2018) 397–416.

24

[4] A. Giusti, E. Mastorakos, Detailed chemistry LES/CMC simulation of a swirling ethanol spray flame approaching blow-off, Proceedings of the Combustion Institute 36 (2017) 2625–2632.

[5] D. Noh, S. Gallot-Lavallée, W. P. Jones, S. Navarro-Martinez, Comparison of droplet evaporation models for a turbulent, non-swirling jet flame with a polydisperse droplet distribution, Combustion and Flame 194 (2018) 135–151.

[6] A. Stagni, L. Esclapez, P. Govindaraju, A. Cuoci, T. Faravelli, M. Ihme, The role of preferential evaporation on the ignition of multicomponent fuels in a homogeneous spray/air mixture, Proceedings of the Combustion Institute 36 (2017) 2483–2491.

[7] P. B. Govindaraju, T. Jaravel, M. Ihme, Coupling of turbulence on the ignition of multicomponent sprays, Proceedings of the Combustion Institute 37 (2019) 3295–3302.

[8] G. Eckel, J. Grohmann, L. Cantu, N. Slavinskaya, T. Kathrotia, M. Rachner, P. L. Clercq, W. Meier, M. Aigner, LES of a swirl-stabilized kerosene spray flame with a multi-component vaporization model and detailed chemistry, Combustion and Flame 207 (2019) 134–152.

[9] D. Ballal, A. Lefebvre, Flame propagation in heterogeneous mixtures of fuel droplets, fuel vapor and air, Proceedings of the Combustion Institute 18 (1981) 321–328.

[10] S. Hayashi, S. Kumagai, T. Sakai, Propagation velocity and structure

of flames in droplet-vapor-air mixtures, Combustion Science and Technology 15 (1977) 169–177.

[11] A. Neophytou, E. Mastorakos, Simulations of laminar flame propagation in droplet mists, Combustion and Flame 156 (2009) 1627–1640.

[12] B. Rochette, E. Riber, B. Cuenot, Effect of non-zero relative velocity on the flame speed of two-phase laminar flames, Proceedings of the Combustion Institute 37 (2019) 3393–3400.

[13] K. Narayanaswamy, H. Pitsch, P. Pepiot, A component library framework for deriving kinetic mechanisms for multi-component fuel surrogates: Application for jet fuel surrogates, Combustion and Flame 165 (2016) 288–309.

[14] E. Ranzi, A. Frassoldati, R. Grana, A. Cuoci, T. Faravelli, A. Kelley, C. K. Law, Hierarchical and comparative kinetic modeling of laminar flame speeds of hydrocarbon and oxygenated fuels, Progress in Energy and Combustion Science 38 (2012) 468–501.

[15] P. Pepiot, Automatic strategies to model transportation fuel surrogates, Ph.D. thesis, Stanford University, Department of Mechanical Engineering, 2008.

[16] B. Rauch, R. Calabria, F. Chiariello, P. Le Clercq, P. Massoli, M. Rachner, Accurate analysis of multicomponent fuel spray evaporation in turbulent flow, Experiments in fluids 52 (2012) 935–948.

[17] I. Javed, S. W. Baek, K. Waheed, G. Ali, S. O. Cho, Evaporation

characteristics of kerosene droplets with dilute concentrations of ligand-protected aluminum nanoparticles at elevated temperatures, Combustion and flame 160 (2013) 2955–2963.

List of supplementary material

Supplementary_Material_S1.xlsx contains:

Reduced ARC mechanism JetA_3Comp_45_686_16_QC